***Supporting Information***

# Interconnected Ni nanowires integrated with $Li_xMnO_2$ as fast charging and high volumetric capacity cathodes for Li-ion batteries

Stanislaw P. Zankowski[a,b *], Diana Chaykina[c] and Philippe M. Vereecken[a,b]

[a] imec, Kapeldreef 75, Leuven 3001, Belgium

[b] M2S Department, Centre for Surface Chemistry and Catalysis, University of Leuven (KU Leuven), Kasteelpark Arenberg 23, Leuven 3001, Belgium

[c] Faculty of Engineering Science, University of Leuven (KU Leuven), Kasteelpark Arenberg 1, Leuven 3001, Belgium

[*]E-mail: st.zankowski@gmail.com

## Supporting text

### XPS analysis of electrodeposited $MnO_2$

The chemical state of the deposited EMD was assessed with X-ray Photoemission Spectroscopy (XPS) (Figure S2). The Mn 2p spectrum shows the $2p_{3/2}$ peak centred at 642.2 eV and separated from the $2p_{1/2}$ peak by 11.6 eV, which agrees with the values for $MnO_2$.[1–3] Furthermore, the O 1s spectrum can be deconvoluted into three peaks at 529.7 eV, 531.1 eV and 531.7 eV, corresponding to the oxygen in the oxide (Mn-O-Mn), hydroxide (Mn-OH) and chemisorbed water, respectively.[4,5] Both the separation between the oxide O 1s peak and the Mn $2p_{3/2}$ maximum of 112.5 eV and the background-corrected intensity ratio of these two peaks of 1.4 are also in agreement with the data for $MnO_2$.[2,3] The O 1s components for -OH and H-OH are indicative to the presence of structural water,[6,7] whose molecular content can be estimated as 0.7 per molecule of $MnO_2$. The structural water lowers crystallinity of nanoscale $MnO_2$,[8] resulting in the absence of $MnO_2$-specific peaks in the X-ray diffraction (XRD) spectrum (Figure 4b in the article). Lack of XRD peaks is also consistent with previous observations for EMD deposited at room temperature.[9,10]

### Thermodynamic calculations of solid-state $MnO_2$ lithiation

In order to examine synthetic routes of LMO within the temperature budget of the nanomesh, we compared temperature-dependent Gibbs free energies of reactions of $MnO_2$ with three common lithium precursors: LiOH, $Li_2CO_3$ and $LiNO_3$. As for the products, at least 7 different LMO's are currently known;[11] for our calculations we considered three of them which are commonly reported as the products of thermal lithiation of $MnO_2$: spinel $LiMn_2O_4$, layered $LiMnO_2$ and layered $Li_2MnO_3$ (other types of LMO such as spinel $Li_4Mn_5O_{12}$ were not considered due to the lack of available thermodynamic data). For example, for a spinel $LiMn_2O_4$ product, the reactions could be written as:

$$8MnO_2 + 4LiOH \rightarrow 4LiMn_2O_4 + 2H_2O_{(g)} + O_{2\,(g)} \quad \text{(S1)}$$

$$8MnO_2 + 2Li_2CO_3 \rightarrow 4LiMn_2O_4 + 2CO_{2\,(g)} + O_{2\,(g)} \quad \text{(S2)}$$

$$4MnO_2 + 2LiNO_3 \rightarrow 2LiMn_2O_4 + \begin{cases} 2NO_{2\,(g)} + O_{2\,(g)} & \text{(S3a)} \\ 2NO_{\,(g)} + 2O_{2\,(g)} & \text{(S3b)} \\ N_2O_{\,(g)} + 2.5O_{2\,(g)} & \text{(S3c)} \\ N_{2\,(g)} + 3O_{2\,(g)} & \text{(S3d)} \end{cases}$$

The results are presented in Figure S3. At moderately low temperatures, the thermal lithiation of $MnO_2$ is most thermodynamically favourable using LiOH as the lithium precursor, as evident from the most negative change of Gibbs free energy ($\Delta G$) for all three types of LMO products. Indeed, synthesis of $LiMnO_2$ using solid LiOH was previously demonstrated at low temperature of 300 ºC.[12] Although oxidation of Ni with $MnO_2$ shows even more negative change of Gibbs free energy in the entire temperature range, for the nanomesh it is kinetically limited up to about 260 ºC, as established previously. As for the reaction of $MnO_2$ with $Li_2CO_3$, the equilibrium calculations predict only a slight tendency towards formation of $LiMn_2O_4$ below 300 ºC, which is in general agreement with experimental observations of Ogata *et al.*[13] When $LiNO_3$ is considered as a lithium precursor, its reaction with $MnO_2$ can proceed through different pathways, with a formation of $NO_2$, NO, $N_2O$ or $N_2$ (or their combination) as the by-products of decomposition of $LiNO_3$.[14–16] Unless the total decomposition of nitrate to $N_2$ is assumed (i.e. Reaction (S3d)), the reactions of $MnO_2$ with $LiNO_3$ are thermodynamically unfavourable in the low-to-moderate temperature range, as expressed by the positive values of $\Delta G$. In practice, Kumagai *et al.* showed that reacting $MnO_2$ with $LiNO_3$ at the melting point of $LiNO_3$ of 260 ºC can give electrochemically active $Li_xMnO_2$ ($0 \leq x \leq 1$) after 7 days of reaction.[17] The activation of the nanomesh cathodes was thus tested using LiOH as the lithium precursor.

*Method for thermodynamics calculations*

The calculations of Gibbs free energies of reactions were carried out using HSC Chemistry 9.6.1 from Outotec. The Gibbs free energies of reactions are calculated as the difference between the Gibbs free energies of formation of the products and substrates. For each species, Gibbs free energy of formation at a given temperature is calculated using equation:

$$\Delta G_f(T) = \Delta H_f(T) - \Delta S_f(T) \cdot T \tag{S4}$$

where $\Delta G_f(T)$ is the Gibbs free energy of formation at the temperature $T$ and $\Delta H_f(T)$ and $\Delta S_f(T)$ are the enthalpy and entropy of formation from pure elements in their standard form, respectively.

The enthalpy of formation of a compound is calculated knowing its standard enthalpy of formation at 298.15 K and pressure of 1 bar ($\Delta H_f^0$) and the integrated molar heat capacity of the compound ($C_p$):

$$\Delta H(T) = \Delta H_f^0(298.15\text{K}) + \int_{298.15K}^{T} C_p(T)dT + \Delta H_{tr} \tag{S5}$$

where $\Delta H_{tr}$ is the enthalpy of phase transition (if applicable).

The entropy of formation of a compound is calculated as the difference between the absolute entropy of the compound and the absolute entropies of the constituent elements in their standard form. For each species, the absolute entropy at any given temperature is calculated from its standard absolute entropy at 298.15K and 1 bar ($S^0$) and the heat capacity of the compound or element at that temperature:

$$S(T) = S^0(298.15\text{K}) + \int_{298.15K}^{T} \frac{C_p(T)}{T} dT + \frac{\Delta H_{tr}}{T_{tr}} \tag{S6}$$

where $T_{tr}$ is the temperature of phase transition (if applicable).

Therefore, to perform the calculations, the necessary input for each compound and the

constituent elements is their $\Delta H_f^0$, $S^0$, $\Delta H_{tr}$ and $T_{tr}$ (if applicable) and $C_p$ as a function of $T$ (note that for pure elements, $\Delta H_f^0 = 0$). The $C_p(T)$ is tabulated in a form of coefficients A-F used to calculate $C_p$ from the polynomial:

$$C_p(T) = A + BT \times 10^{-3} + CT^{-2} \times 10^5 + DT^2 \times 10^{-6} + ET^{-3} \times 10^8 + FT^3 \times 10^{-9} \quad \text{(S7)}$$

Since the necessary thermodynamic parameters for $MnO_2$, LiOH, $Li_2CO_3$, $LiNO_3$ and the constituent elements are already included in the default HSC Chemistry database, we provide only those for lithiated manganese oxides, which we compiled from the literature (Table S1). The standard Gibbs free energies of formation of the compounds are presented in Table S2.

**Note on the phase composition of synthesized samples**

The XRD diffractograms of all the annealed samples (Figure 4b in the article) show a broad peak centred at about 18.3°, the intensity of which increases with the temperature of thermal lithiation. Such peak can be ascribed to the monoclinic $LiMnO_2$ ($2\theta_{001}$ = 18.3°), but is also close to the diffraction peak of spinel forms of LMO (e.g. $LiMn_2O_4$ or $Li_4Mn_5O_{12}$, $2\theta_{111}$ = 18.6 – 18.8°) or of the layered $Li_2MnO_3$ ($2\theta_{002}$ = 18.7°) (ICDD PDF cards #87-1255, #35-0782, #46-0810 and #27-1252, respectively). However, the low cyclic voltammetry activity of the samples in the 4 V region[18,19] suggests a little presence of electrochemically active spinel LMO's. Furthermore, the observed electrochemical activity does not come from $Li_2MnO_3$, since $Li_2MnO_3$ is electrochemically inactive in the potential window of 4.4 – 2.2 V unless previously de-lithiated at a high voltage of about 4.8 V vs. $Li^+/Li$.[20–22] Also, when cycled up to 5 V, we did not observe the irreversible anodic peak characteristic to the activation of $Li_2MnO_3$.[20,21] These observations support the proposed composition of lithium-deficient $Li_xMnO_2$, which was also previously suggested as the product of reaction of $MnO_2$ with LiOH at low temperatures.[23,24]

***In-situ* conversion of $MnO_2$ during ALD of $LiOH/Li_2O$**

Besides impregnating the $MnO_2$-coated nanomesh with drop-cast aqueous LiOH and annealing, we also attempted to facilitate the conversion of $MnO_2$ to the high-voltage spinel LMO's (e.g. $LiMn_2O_4$) *in-situ* during thermal atomic layer deposition (ALD) of $LiOH/Li_2O$, performed at the conversion temperature of $MnO_2$ and over an extended time. This technique utilizes vapours of metalorganic precursors that can penetrate porous materials and precisely coat their internal pores (as small as ~1 nm, depending on the size of precursor molecules) with solid layers of e.g. $TiO_2$.[25,26] In our case, thermal ALD was performed for 72 hours at 250 °C (the highest temperature at which the nanomesh does not oxidize), using vapours of lithium tert-butoxide and water as the ALD precursors. Such ALD process produces LiOH, which at 250 °C can simultaneously decompose into $Li_2O$ with hydroxylated surfaces.[27] We suspected that employing ALD could facilitate the synthesis of spinel LMO through: a) the high activity and diffusivity of Li tert-butoxide molecules in the gas phase, b) the high contact area between $MnO_2$ surfaces and ALD-deposited $LiOH/Li_2O$, c) the extended time of processing at 250 °C. Compared to the analogous electrode obtained from drop-cast LiOH and annealing for 2 h, ALD gave an electrode with sharper voltammetry peaks in the 3 V region and more distinguishable, small peaks at about 4.1 V (Fig. S6a). Nevertheless, the absolute CV currents in the 4 V region remained low, showing that no significant amount of spinel LMO was formed. Also, during discharge-charge cycles at various C-rates, the ALD-LiOH electrode showed discharge capacities close to these of the shortly annealed sample prepared from aqueous LiOH (Fig. S6b; note that the difference between capacities at low currents falls within the sample-to-sample variability of ~10%). We can note, however, that the ALD-LiOH electrode reached relatively higher capacity at high currents with respect to its capacity at low currents. Tentatively, the differences in electrochemical performance of the two electrodes can be due to

different degree of crystallization of $Li_xMnO_2$ prepared during 72 h of ALD annealing, as compared to the $Li_xMnO_2$ prepared during 2 h of annealing with drop-cast LiOH.

The conversion during ALD of LiOH/$Li_2O$ was performed inside the Picosun ALD R200 reactor integrated with an Ar-filled glovebox. The deposition was carried out at the temperature of 250 °C and the pressure of 14 mbar, using Li tert-butoxide and water vapor as the growth precursors and Ar as the carrier and purging gas. The growth was conducted for 150 ALD cycles, each consisting of a pulse of Li tert-butoxide at 150 sccm for 140 s, 500 s purge, a pulse of $H_2O_{(g)}$ at 200 sccm for 80 s and 1000 s purge. During the deposition, the Li tert-butoxide container was heated to 140 °C and to 165 °C on the valve-block while the $H_2O$ source was maintained at 18 °C. After the deposition, the sample was immersed in $H_2O$ for 10 min and dried in air at 120 °C for 12 h.

**Conversion of $MnO_2$ with Li isopropoxide and Li citrate**

Besides testing the conversion of $MnO_2$ with LiOH, we assessed Li isopropoxide and Li citrate as the alternative Li precursors. Lithium isopropoxide is a solid which at atmospheric pressure sublimes at about 230 °C, hydrolyzing to LiOH upon contact with water. Lithium citrate is a precursor used in sol-gel synthesis of LMO, which was also reported to convert EMD to spinel $LiMn_2O_4$ at temperatures as low as 280 °C.[28,29] For the conversion using Li isopropoxide, the sample was placed on a hotplate in a glovebox. On the same hotplate, next to the sample, a pinch of Li isopropoxide powder (95%, Sigma Aldrich) was placed and both the sample and the powder were covered with a watch glass. The reaction was conducted for 2 hours at 250 °C, as set on the hotplate. After that time, the sample was removed from the glovebox, transported in air to a $N_2$-filled oven and annealed for another 2 hours at 250 °C. After that, the sample was placed in a $H_2O$-filled beaker for 10 min, washed under running water and dried with $N_2$ blow.

A sol of lithium citrate was made by preparing a solution of 3 M lithium hydroxide (≥98%, Sigma Aldrich), 1 M citric acid (99.5%, Sigma Aldrich) and 0.01% wt. Pluronic F-127 (Sigma Aldrich) as a single mixture in water. 20 μL of this solution were drop cast onto the $MnO_2$-coated nanomesh electrode and dried with a steady steam of $N_2$. The sample was annealed in air at 250 °C using a Thermo Scientific Type F6000 Furnace. The ramp-up phase of the annealing was thoroughly optimized to avoid rapid gas evolution from the decomposing citrate. The ramp-up phase consisted of three isothermal steps: 90 °C for 1h, 120 °C for 6 h, 160 °C for 6 h, followed by the final anneal at 250 °C for 12 h. The heating rate during the ramp-up was set at 10 $^{o}$C/min. After the annealing and cooling down, the sample was placed in a $H_2O$-filled beaker for 10 min, washed under running water and dried with $N_2$ blow. The voltammetric response of both types of samples is presented in Fig. S6a.

While the isopropoxide gave electrodes with a similar voltammetric response to the ones obtained from LiOH, lithium citrate was the only precursor to yield electrodes with a distinguishable pair of spinel-like voltammetric peaks in the 4 V region. The absolute currents in the citrate-processed samples were, however, much lower than in the other samples, which could be due to some damage of the electrode structure by the excessive gas evolution during thermal decomposition of the citrate or due to the presence of insoluble residues within the electrode which were observed with SEM after the conversion and washing.

**Notes on the comparison of 3D cathodes reported in the literature**

Table S3 presents data on volumetric capacities, high rate performance and volume loading of active materials in various 3D-nanostructured core-shell electrodes reported in the literature. If not explicitly reported in an article, the fractions of electrode volume occupied by active materials ($VF_{act}$) were calculated according to equation:

$$VF_{act} = L_{act} / \rho_{act} \quad \text{(S8)}$$

where $L_{act}$ is the active material loading (in g/cm$^3$, according to electrode thickness and superficial loading of active material, typically reported in mg/cm$^2$) and $\rho_{act}$ is the crystal density of the active material: $\rho_{LiMnO2}$ = 3.89 g/cm$^3$, $\rho_{MnO2}$ = 4.74 g/cm$^3$ (averaged density of different polymorphs of $MnO_2$), $\rho_{LiCoO2}$ = 5.05 g/cm$^3$, $\rho_{V2O5}$ = 3.36 g/cm$^3$.

The theoretical currents at 1 C are the currents required for complete removal/insertion of $Li^+$ in the active materials in 1 hour of reactions:

$$Li^+ + CoO_2 + e^- \rightleftarrows LiCoO_2 \qquad 274\ \text{mAh/g}_{LiCoO2} \tag{S9}$$

$$Li^+ + MnO_2 + e^- \rightleftarrows LiMnO_2 \qquad 285\ \text{mAh/g}_{LiMnO2}\ (\text{for } MnO_2, Li_xMnO_2 \text{ and } LiMnO_2) \tag{S10}$$

$$2Li^+ + MnSiO_4 + 2e^- \rightleftarrows Li_2MnSiO_4 \qquad 333\ \text{mAh/g}_{Li2MnSiO4} \tag{S11}$$

$$2Li^+ + 2MnO_2 + 2e^- \rightleftarrows Li_2Mn_2O_4 \qquad 296\ \text{mAh/g}_{LiMn2O4} \tag{S12}$$

(spinel $LiMn_2O_4$ cycled between 4.5 and 2.5 V vs. $Li^+$/Li)

$$2Li^+ + V_2O_5 + 2e^- \rightleftarrows Li_2V_2O_5 \qquad 294\ \text{mAh/g}_{V2O5} \tag{S13}$$

(in the studied potential range in refs.,[30,31] down to 2.0 V vs. $Li^+$/Li)

## Supporting tables

**Table S1.** Thermodynamic parameters of three LMO's used for thermodynamic calculations

| Compound | $\Delta H^0$ (kJ/mol) | $S^0$ (J/(Kmol)) | A | B | C | D | E | F |
|---|---|---|---|---|---|---|---|---|
| m-$LiMnO_2$* | -828.70[32] | 78.28‡ | -14.361 | 546.961 | -0.239 | -913.381 | 0.007 | 521.827 |
| $LiMn_2O_4$** | -1381.65[33] | 133.70[34] | 154.513 | 89.929 | -38.469 | -102.414 | 4.394 | 61.706 |
| $Li_2MnO_3$† | -1233.05[35] | 107.22‡ | 136.850 | 22.400 | -31.220 | 0.000 | 0.000 | 0.000 |

*For m-$LiMnO_2$, the heat capacity coefficients (A-F) were fitted from isobaric heat capacities ($C_p$) calculated from the isochoric heat capacities ($C_v$) reported in ref.[36], according to equation $C_p = C_v + \beta^2 BVT$, where $\beta$ is the coefficient of volumetric thermal expansion (taken as $5.64\times10^{-5}$ 1/K),[37] $B$ is the bulk modulus (102 GPa),[38] $V$ is the unit cell volume (38.406 Å$^3$)[38] and $T$ is temperature.
**For $LiMn_2O_4$, the heat capacity coefficients were fitted from the coefficients reported in Table 3 in ref. [39]
†For $Li_2MnO_3$, the heat capacity coefficients were fitted from the $C_p$ values reported in ref. [35]
‡Estimated with HSC Estimate Module v. 9.6.1

**Table S2.** Standard Gibbs free energies of formation

| Compound | $\Delta G_f^0$ (kJ/mol) |
|---|---|
| m-$LiMnO_2$ | -771.83 |
| $LiMn_2O_4$ | -1271.29 |
| $Li_2MnO_3$ | -1146.30 |
| $MnO_2$ | -465.12 |
| LiOH | -438.92 |
| $Li_2CO_3$ | -1132.10 |
| $LiNO_3$ | -384.713 |
| $H_2O_{(g)}$ | -228.58 |
| $CO_{2(g)}$ | -394.36 |
| $NO_{2(g)}$ | +51.18 |
| $NO_{(g)}$ | +86.61 |
| $N_2O_{(g)}$ | +103.72 |

**Table S3.** Properties of some 3D core-shell Li-ion cathodes reported in the literature

| Cathode | $d_{el}$ (µm) [a] | $t_{act}$ (nm) | Discharge capacity @ reported C-rate | Reported current @ 1C | Theoretical current @ 1C | U (V) | Loading (g/cm$^3$) | $VF_{act}$ (%) | $VF_s$ (%) | Ref. |
|---|---|---|---|---|---|---|---|---|---|---|
| This work | 3.3 | 12 ± 2 | 214 mAh/cm$^3$ @ 1.2 C [b]<br>94 mAh/cm$^3$ @ 24 C [b] | 26.8 A/mol Mn =<br>269 mA/cm$^3$ | 26.8 A/mol Mn =<br>269 mA/cm$^3$ | 3.0 | ~0.78<br>($LiMnO_2$) | 25 ± 10 | 24 | - |
| $Li_2MnSiO_4$/IO | N/A | 150-200 | 298 mAh/cm$^3$ @ 0.8 C<br>191 mAh/cm$^3$ @ 1.6 C | 333 mA/$g_{act}$ ≈<br>1231 mA/cm$^3$ [c] | 333 mA/$g_{act}$ | 3.2 | 2.8 | 90 | <10 | 40 |
| $Li_xMnO_2$/IO | N/A | 30 | 198 mAh/$g_{act}$ @ 1.1 C<br>76 mAh/$g_{act}$ @ 1114 C | 198 mAh/$g_{act}$ [c] | 285 mA/g $_{LiMnO2}$<br>~308 mA/g $_{MnO2}$ | 3.0 | N/A | N/A | 6 | 41 |
| $MnO_2$/CNT | 60 | 6.5 | 108 mAh/cm$^3$ @ 0.1 C [d]<br>33 mAh/cm$^3$ @ 20 C [d] | 150 mA/$g_{act}$ ≈<br>52.5 mA/cm$^3$ [d] | 308 mA/$g_{act}$ ≈<br>108 mA/cm$^3$ | 3.0 | 0.35 | 7 | N/A | 42 |
| $LiMn_2O_4$/Si µp | ~55 | ~250 | 85 mAh/cm$^3$ @ 0.1 C<br>51 mAh/cm$^3$ @ 10 C | 370 µA/cm$^2$ ≈<br>67 mA/cm$^3$ | 1270 mA/$g_{act}$<br>83 mA/cm$^3$ [e] | 3.5 | 0.02 [f] | 7 [f] | ~30 | 28 |
| $LiCoO_2$/Al NWs | 8 | 30 | ~156 mAh/cm$^3$ @ 0.03 C<br>~104 mAh/cm$^3$ @ 8 C | ~156 mA/cm$^3$ | N/A | 3.8 | N/A | N/A | ~40 | 43 |
| $LiCoO_2$/C fiber | 130 | 270-980 | 82 mAh/cm$^3$ @ 0.1 C<br>62 mAh/cm$^3$ @ 2 C | 274 mA/$g_{act}$ ≈<br>192 mA/cm$^3$ | 274 mA/$g_{act}$ ≈<br>192 mA/cm$^3$ | 3.9 | 0.72 | 14 | 18 | 44 |
| $LiCoO_2$/C foam | 500 | N/A | 401 mAh/cm$^3$ @ 0.05 C<br>303 mAh/cm$^3$ @ 2 C | 137 mA/$g_{act}$ ≈<br>397 mA/cm$^3$ [c] | 274 mA/$g_{act}$ ≈<br>795 mA/cm$^3$ | 3.9 | 2.9 | 57 | 15 | 45 |
| $LiCoO_2$/CNF | 100 | ~125 | 110 mAh/cm$^3$ @ 0.5 C<br>85 mAh/cm$^3$ @ 50 C | 137 mA/$g_{act}$ ≈<br>110 mA/cm$^3$ [c] | 274 mA/$g_{act}$ ≈<br>215 mA/cm$^3$ | 3.9 | 0.81 [f] | 16 [f] | N/A | 45 |
| $V_2O_5$/CNT/PAN | 57 | < 100 | 178 (139) mAh/cm$^3$ @ 0.5 C [g]<br>126 (96) mAh/cm$^3$ @ 5 C | 300 mA/$g_{act}$ ≈<br>150 mA/cm$^3$ | 294 mA/$g_{act}$ ≈<br>152 mA/cm$^3$ | 3.0 | 0.51 [h] | 15 | N/A | 30 |

**Table S3.** Continued

| Cathode | $d_{el}$ (µm) [a] | $t_{act}$ (nm) | Discharge capacity @ reported C-rate | Reported current @ 1C | Theoretical current @ 1C | U (V) | Loading (g/cm$^3$) | $VF_{act}$ (%) | $VF_s$ (%) | Ref. |
|---|---|---|---|---|---|---|---|---|---|---|
| $V_2O_5$/IO | 6 | 60 | ~243 mAh/cm$^3$ @ 1 C<br>123 mAh/cm$^3$ @ 100 C [i] | 294 mA/$g_{act}$ ≈<br>285 mA/cm$^3$ | 294 mA/$g_{act}$ ≈<br>285 mA/cm$^3$ | 3.0 | 0.94 | 28 | ≤10 | 31 |
| m-$LiMnO_2$ NPs | N/A | 40-60 | 170 mAh/g @ 50 mA/g<br>~66 mAh/g @ 1000 mA/g | N/A | 285 mA/$g_{act}$ | 3.3 | 2 mg/cm$^2$ | N/A | N/A | 46 |

[a] Abbreviations: $d_{el}$ – thickness of 3D electrode, $t_{act}$ – thickness of active material layer, U – average discharge potential at low C-rates, $VF_{act}$ – volume fraction of 3D electrode occupied by active material, $VF_s$ – volume fraction of 3D electrode occupied by 3D substrate, IO – inverse opals, µp – micropillars, NWs – nanowires, CNT – carbon nanotubes, PAN – polyacrylonitrile nanofibers, CNF – carbon nanofibers, NPs – nanoparticles
[b] averaged from five discharge-charge cycles at 24 C
[c] based on the correspondence with the first author
[d] based on the reported gravimetric capacities, electrode thickness and averaged loading of $MnO_2$ of 2.1 mg/cm$^2$
[e] based on the claim that the capacity recorded at 10 C corresponds to 61% of theoretical capacity
[f] inferred from the discharge capacity at the lowest C-rate
[g] The authors report gravimetric capacity of 149 mAh/$g_{cathode}$ corresponding to volumetric capacity of 178 mAh/cm$^3$. However, calculating volumetric capacity using the reported electrode thickness (57 µm), superficial cathode density (5.2 mg/cm$^2$) and gravimetric capacity gives volumetric capacity of 139 mAh/cm$^3$. We have asked the authors for clarification of this discrepancy but received no response up to date. Thus, next to the original volumetric capacities, we give in parenthesis the values calculated according to the reported electrode dimensions, density and gravimetric capacity.
[h] based on the reported $V_2O_5$ mass fraction of 56%, electrode thickness and superficial cathode density.
[i] based on the reported relationship between gravimetric and volumetric capacities

## Supporting figures

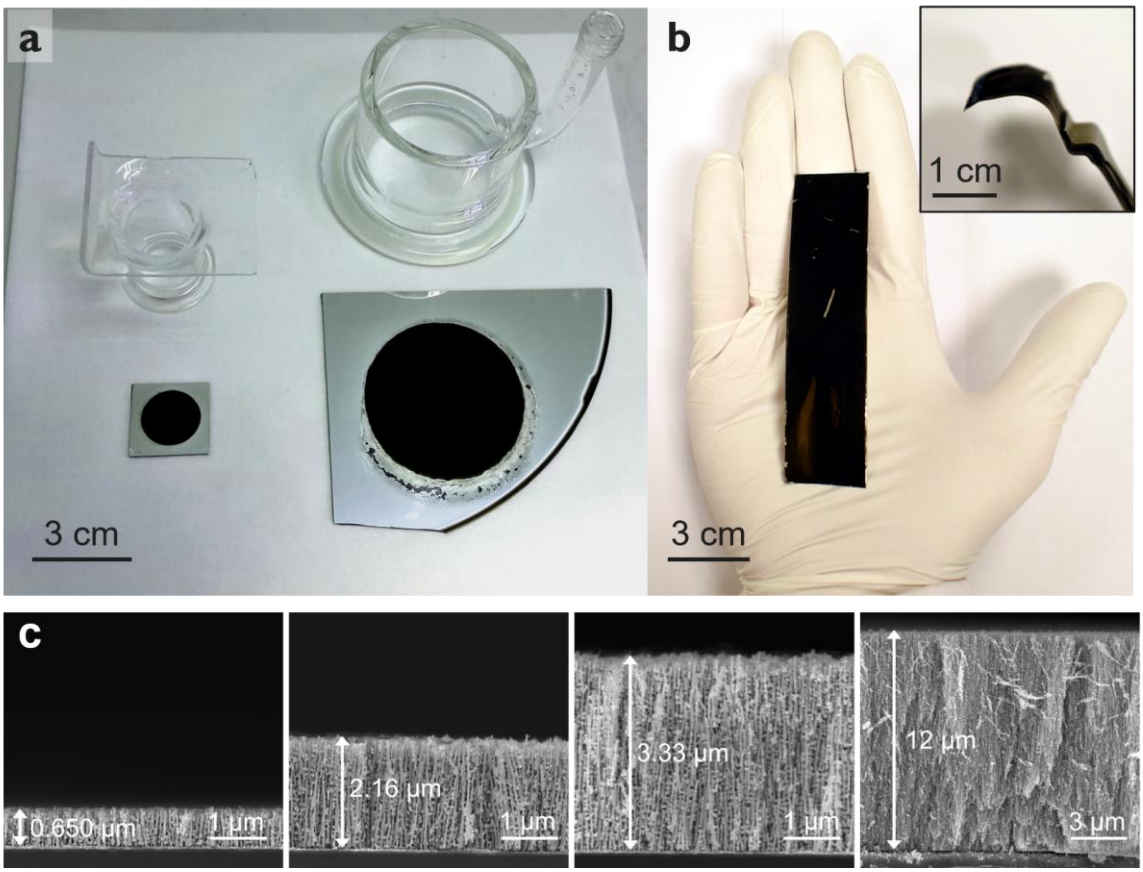


**Fig. S1** Up-scalable character of the Ni nanomeshes in area, shape and thickness. (a) Photograph of two circular wafer-supported nanomeshes with 2.5 $cm^2$ and 25 $cm^2$ footprint area (black area in the middle of each wafer), prepared using electrochemical cells with different window size (shown above the wafers); (b) Photograph of a free-standing rectangular nanomesh foil, also showing the flexibility of the free-standing nanomesh foil (inset); (c) SEM images of nanomeshes with increasing network thicknesses. The thickness of the nanomesh can be precisely adjusted by changing the time of Ni electrodeposition.

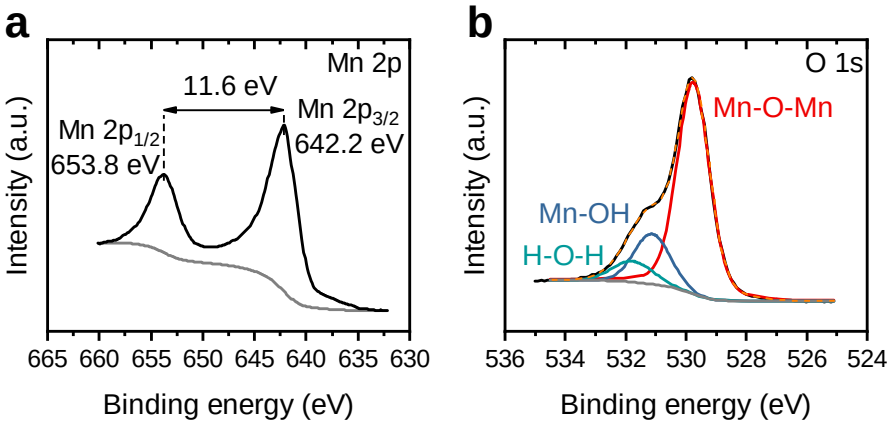


**Fig. S2** XPS spectra of $MnO_2$. (a) Mn 2p spectrum; (b) O 1s spectrum. The content of structural water (-OH and H-OH) in the material was calculated as $2n(1-n)^{-1}$, where $n$ is the sum of relative contributions of the -OH and H-OH peak areas to the overall O 1s spectrum.

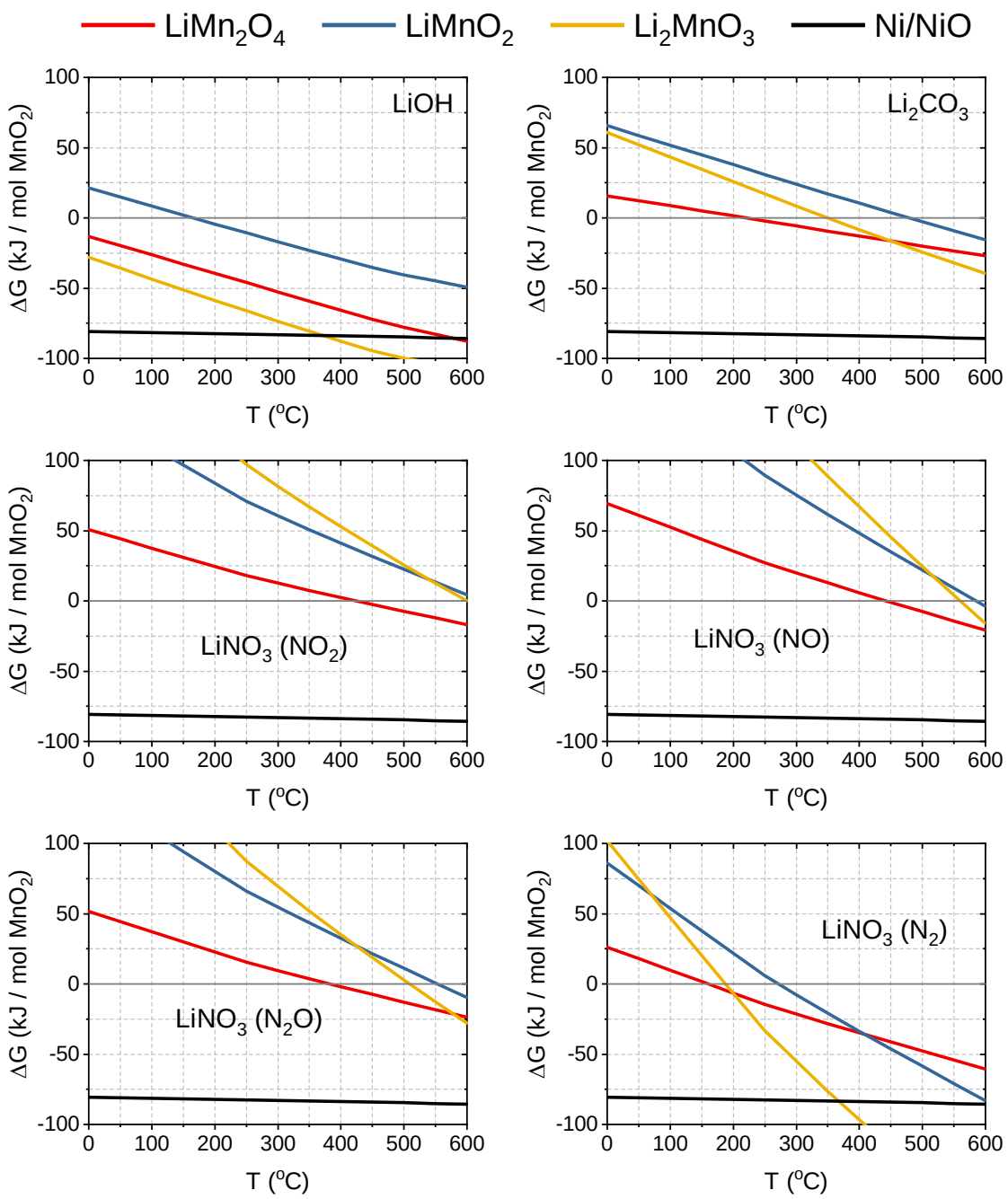


**Fig. S3** Calculated Gibbs free energies of formation of $LiMn_2O_4$, $LiMnO_2$ and $Li_2MnO_3$ through reaction of $MnO_2$ with LiOH, $Li_2CO_3$ and $LiNO_3$. For $LiNO_3$, the reactions were considered for different gaseous reduction products ($NO_2$, NO, $N_2O$ and $N_2$). The Gibbs free energy of oxidation of Ni with $MnO_2$ is also given (Ni/NiO).

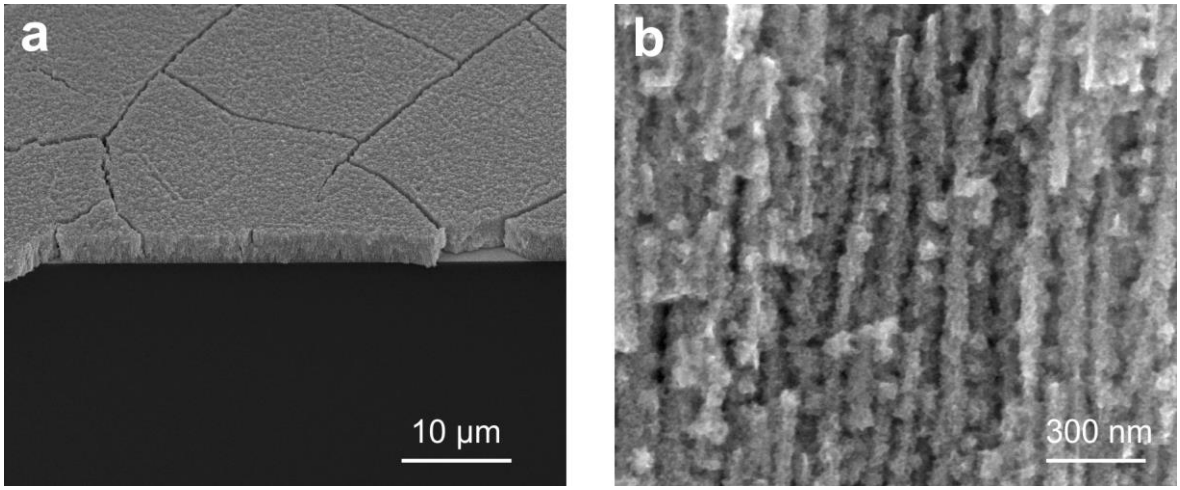


**Fig. S4** SEM images of the $Li_xMnO_2$-coated nanomesh electrode made by impregnation with LiOH, annealing at 250 $^oC$ and washing with water. (a) Low magnification image taken at 45$^o$ angle, (b) High magnification cross section image.

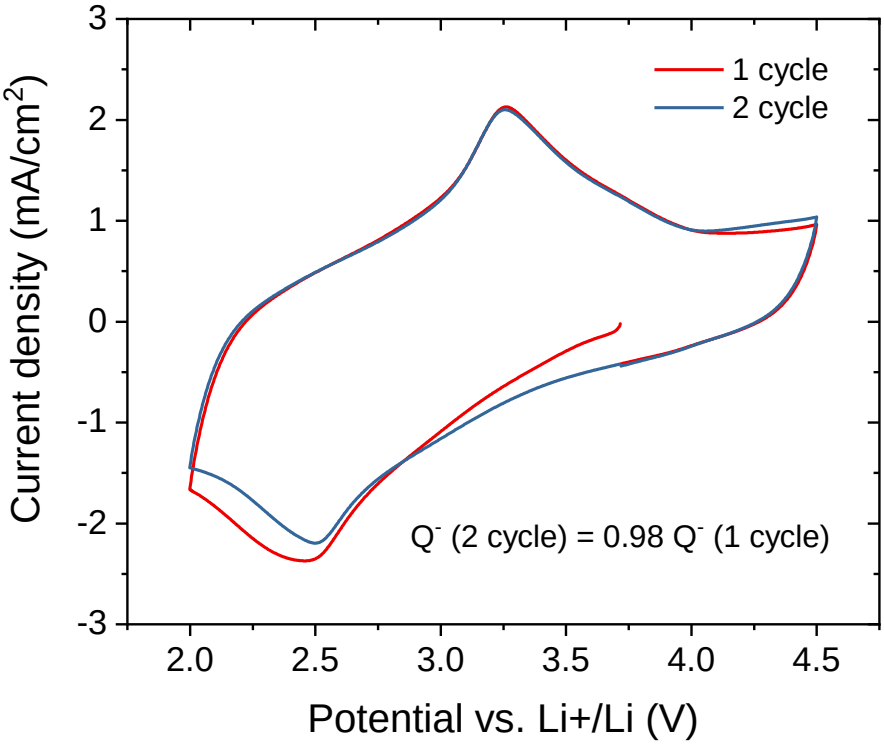


**Fig. S5.** Cyclic voltammograms of nanomesh cathode prepared from drop-cast LiOH annealed at 250 $^oC$, showing first and second CV scan. The large cathodic peak in the initial negative scan indicates lithium insertion into the as-synthesized, mostly lithium-free $Li_xMnO_2$ (the integrated cathodic charge recorded in the second CV cycle was 0.98 of the cathodic charge in the first cycle). The voltammograms were recorded in 1 M $LiClO_4$ / propylene carbonate at 10 mV/s.

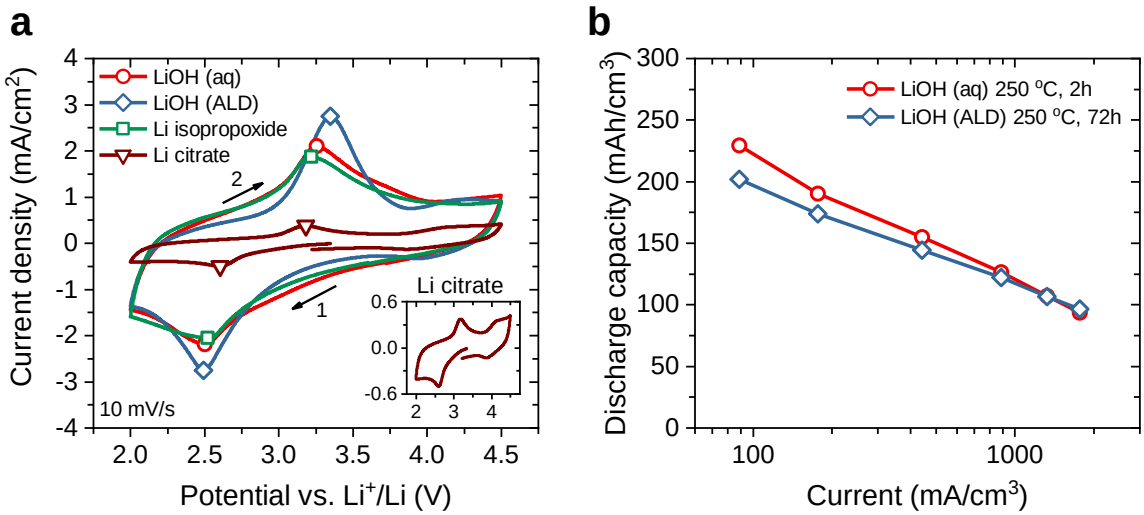


**Fig. S6.** Electrochemistry of $Li_xMnO_2$/nanomesh electrodes prepared from different precursors and methods. (a) Cyclic voltammetry, (b) Mean discharge capacity recorded at various currents between 4 and 2 V vs. $Li^+$/Li on electrodes prepared from drop-cast and ALD-deposited LiOH. For each current, five discharge-charge cycles were recorded, and the capacities averaged. The electrochemical measurements were performed in 1 M solution of $LiClO_4$ in propylene carbonate. The electrode prepared from drop-cast LiOH was annealed in $N_2$ at 250 °C for 2 h and the electrode prepared through ALD deposition of LiOH was processed in Ar at 250 °C for 72 h. The electrode prepared from Li isopropoxide was annealed in Ar for 2 h at 250°C, followed by annealing in $N_2$ for 2 h. The electrode prepared from drop-cast Li citrate was annealed in air at 250 °C for 12 h.

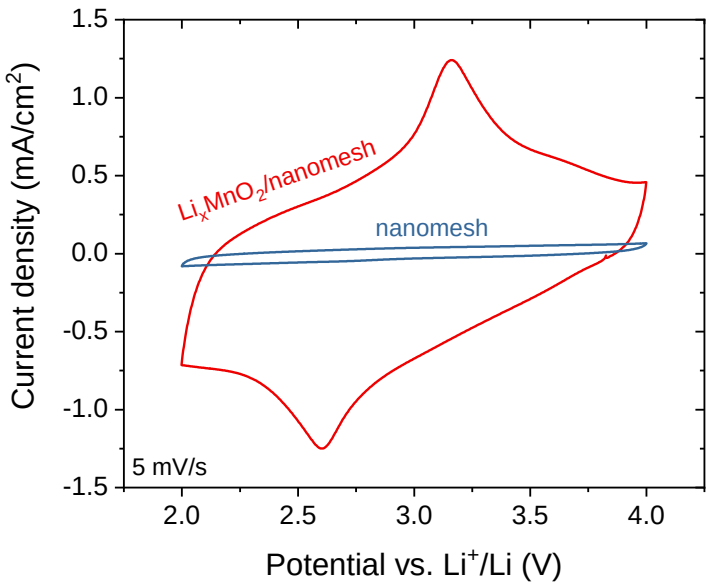


**Fig. S7.** Cyclic voltammograms of the $Li_xMnO_2$-coated nanomesh and of a nanomesh with thermally oxidized surface. The ratio between the charges recorded on the bare and $Li_xMnO_2$-coated nanomesh of 0.06 was used for subtracting capacity due to background processes from the recorded capacities on the nanomesh cathodes.

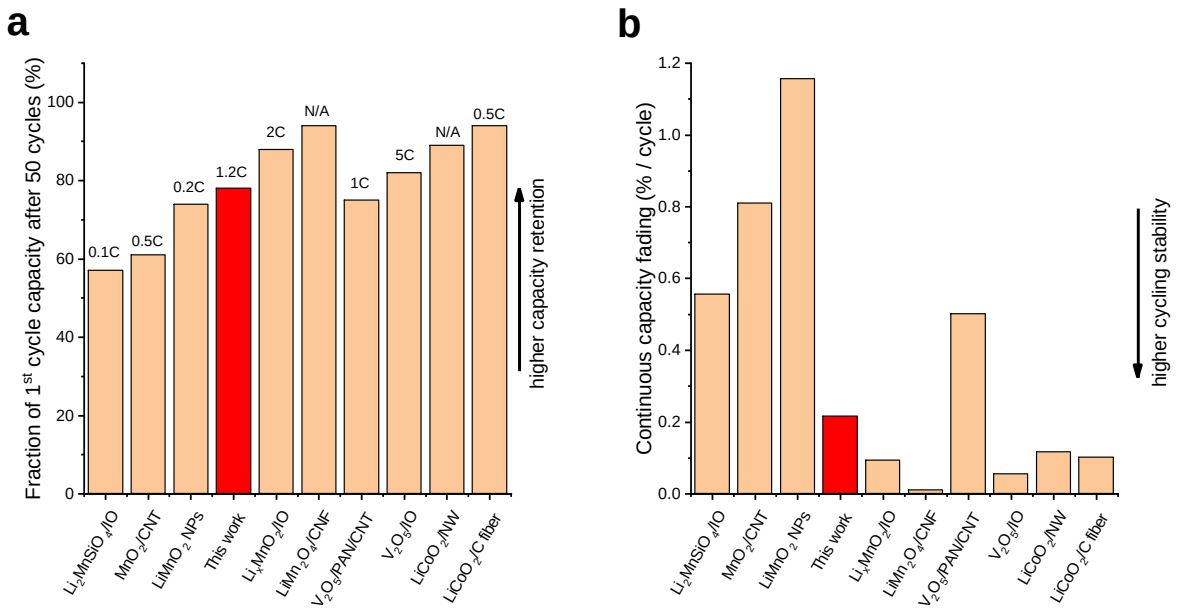


**Fig. S8.** Stability of $Li_xMnO_2$/nanomesh and other 3D-nanostructured core-shell electrodes reported in the literature. (a) Capacity retention after 50 cycles with respect to the first cycle capacity; (b) Capacity fading during continuous cycling. The nominal C-rates (C-rates based on estimated maximum theoretical capacities) at which the measurements were performed are presented in (a). The capacity fade in (b) was calculated from the relation $a/C_{40}$, where $a$ is the linear slope of the capacity change between 40$^{th}$ and 50$^{th}$ cycle and $C_{40}$ is the capacity at 40$^{th}$ cycle. The literature data was graphically extracted using WebPlotDigitizer. The references are presented in Table S3.

# Bibliography


(1) Di Castro, V.; Polzonetti, G. XPS Study of MnO Oxidation. *J. Electron Spectros. Relat. Phenomena* **1989**, *48*, 117–123.

(2) Foord, J. S.; Jackman, R. B.; Allen, G. C. An X-Ray Photoelectron Spectroscopic Investigation of the Oxidation of Manganese. *Philos. Mag. A Phys. Condens. Matter, Struct. Defects Mech. Prop.* **1984**, *49* (5), 657–663. https://doi.org/10.1080/01418618408233293.

(3) Chigane, M.; Ishikawa, M. Manganese Oxide Thin Film Preparation by Potentiostatic Electrolyses and Electrochromism. *J. Electrochem. Soc.* **2000**, *147* (6), 2246. https://doi.org/10.1149/1.1393515.

(4) Nesbitt, H. W.; Banerjee, D. Interpretation of XPS Mn(2p) Spectra of Mn Oxyhydroxides and Constraints on the Mechanism of MnO2 Precipitation. *Am. Mineral.* **1998**, *83* (3–4), 305–315. https://doi.org/10.2138/am-1998-3-414.

(5) Biesinger, M. C.; Payne, B. P.; Grosvenor, A. P.; Lau, L. W. M.; Gerson, A. R.; Smart, R. S. C. Resolving Surface Chemical States in XPS Analysis of First Row Transition Metals, Oxides and Hydroxides: Cr, Mn, Fe, Co and Ni. *Appl. Surf. Sci.* **2011**, *257* (7), 2717–2730. https://doi.org/10.1016/j.apsusc.2010.10.051.

(6) Dose, W. M.; Donne, S. W. Thermal Treatment Effects on Manganese Dioxide Structure, Morphology and Electrochemical Performance. *J. Electrochem. Soc.* **2011**, *158* (8), A905. https://doi.org/10.1149/1.3597640.

(7) Lee, J. A.; Newnham, C. E.; Tye, F. L. Energetics of Water Desorption from a γ-Manganese Dioxide. *J. Colloid Interface Sci.* **1973**, *42* (2), 372–380. https://doi.org/10.1016/0021-9797(73)90302-0.

(8) Birkner, N.; Navrotsky, A. Thermodynamics of Manganese Oxides: Effects of Particle Size and Hydration on Oxidation-Reduction Equilibria among Hausmannite, Bixbyite, and Pyrolusite. *Am. Mineral.* **2012**, *97* (8–9), 1291–1298. https://doi.org/10.2138/am.2012.3982.

(9) Etman, A. S.; Radisic, A.; Mahmoud, E.; Huyghebaert, C.; Vereecken, P. M.; Emara, M. M.;

Huyghebaert, C.; Vereecken, P. M. Effect of Film Morphology on the Li-Ion Intercalation Kinetics in Anodic Porous Manganese Dioxide Thin-Films. *J. Phys. Chem. C* **2014**, *118* (19), 9889–9898. https://doi.org/10.1021/jp4105008.

(10) Chen, L.; van Zomeren, A.; Schooman, J. Amorphous MnO2 Thin Film Cathode for Rechargeable Lithium Batteries. *Solid State Ionics* **1994**, *67* (3–4), 203–208. https://doi.org/10.1016/0167-2738(94)90006-X.

(11) Thackeray, M. M.; Croy, J. R.; Lee, E.; Gutierrez, A.; He, M.; Park, J. S.; Yonemoto, B. T.; Long, B. R.; Blauwkamp, J. D.; Johnson, C. S.; et al. The Quest for Manganese-Rich Electrodes for Lithium Batteries: Strategic Design and Electrochemical Behavior. *Sustain. Energy Fuels* **2018**, *2* (7), 1375–1397. https://doi.org/10.1039/c8se00157j.

(12) Reimers, J. N.; Fuller, E. W.; Dahn, J. R. Synthesis and Electrochemical Studies of LiMnO2 Prepared at Low Temperatures. *J. Electrochem. Soc.* **1993**, *140* (12), 3396–3401. https://doi.org/10.1149/1.2221101.

(13) Ogata, A.; Shimizu, T.; Komaba, S. Crystallization of LiMn2O4 Observed with High Temperature X-Ray Diffraction. *J. Power Sources* **2007**, *174* (2), 756–760. https://doi.org/10.1016/j.jpowsour.2007.06.150.

(14) McManis, G. E.; Miles, M. H.; Fletcher, A. N. Performance and Discharge Characteristics of Ca/LiCl, LiNO3/LiNO3, AgNO3/Ni Thermal Battery Cells. *J. Electrochem. Soc.* **1984**, *131* (2), 283–286.

(15) Lee, A. K. K.; Johnson, E. F. The Stoichiometry and Kinetics of the Thermal Decomposition of Molten Anhydrous Lithium Nitrite. *Inorg. Chem.* **1972**, *11* (4), 782–787. https://doi.org/10.1021/ic50110a025.

(16) Stern, K. H. High Temperature Properties and Decomposition of Inorganic Salts Part 3, Nitrates and Nitrites. *J. Phys. Chem. Ref. Data* **1972**, *1* (3), 747–772. https://doi.org/10.1063/1.3253104.

(17) Kumagai, N.; Saito, T.; Komaba, S. Synthesis of Ternary Li-Mn-O Phase at a Temperature of 260 °C and Electrochemical Lithium Insertion into the Oxide. *J. Appl. Electrochem.* **2000**, *30* (2), 159–163. https://doi.org/10.1023/A:1003819905672.

(18) Put, B.; Vereecken, P. M.; Labyedh, N.; Sepulveda, A.; Huyghebaert, C.; Radu, I. P.; Stesmans, A. High Cycling Stability and Extreme Rate Performance in Nanoscaled LiMn2O4 Thin Films. *ACS Appl. Mater. Interfaces* **2015**, *7* (40), 22413–22420. https://doi.org/10.1021/acsami.5b06386.

(19) Xie, Z.; Eikhuemelo, H.; Zhao, J.; Cain, C.; Xu, W.; Wang, Y. Ni and Fe Dual-Doped Li4Mn5O12 Spinels as Cathode Materials for High-Voltage Li-Ion Batteries. *J. Electrochem. Soc.* **2015**, *162* (8), A1523–A1529. https://doi.org/10.1149/2.0601508jes.

(20) Saroha, R.; Gupta, A.; Panwar, A. K. Electrochemical Performances of Li-Rich Layered-Layered Li2MnO3-LiMnO2solid Solutions as Cathode Material for Lithium-Ion Batteries. *J. Alloys Compd.* **2017**, *696*, 580–589. https://doi.org/10.1016/j.jallcom.2016.11.199.

(21) Hy, S.; Felix, F.; Rick, J.; Su, W. N.; Hwang, B. J. Direct in Situ Observation of Li2O Evolution on Li-Rich High-Capacity Cathode Material, Li[NixLi(1-2x)/3Mn (2-x)/3]O2 ($0 \leq x \leq 0.5$). *J. Am. Chem. Soc.* **2014**, *136* (3), 999–1007. https://doi.org/10.1021/ja410137s.

(22) Amalraj, S. F.; Sharon, D.; Talianker, M.; Julien, C. M.; Burlaka, L.; Lavi, R.; Zhecheva, E.; Markovsky, B.; Zinigrad, E.; Kovacheva, D.; et al. Study of the Nanosized Li2MnO3: Electrochemical Behavior, Structure, Magnetic Properties, and Vibrational Modes. *Electrochim. Acta* **2013**, *97*, 259–270. https://doi.org/10.1016/j.electacta.2013.03.029.

(23) Thackeray, M. M. Manganese Oxides for Lithium Batteries. *Prog. Solid State Chem.* **1997**, *25* (1), 1–71. https://doi.org/10.1016/S0079-6786(97)81003-5.

(24) Thackeray, M. M.; Rossouw, M. H.; de Kock, A.; de la Harpe, A. P.; Gummow, R. J.; Pearce, K.; Liles, D. C. The Versatility of MnO2 for Lithium Battery Applications. *J. Power Sources* **1993**, *43* (1–3), 289–300. https://doi.org/10.1016/0378-7753(93)80126-A.

(25) Dendooven, J.; Pulinthanathu Sree, S.; De Keyser, K.; Deduytsche, D.; Martens, J. A.; Ludwig, K. F.; Detavernier, C. In Situ X-Ray Fluorescence Measurements during Atomic Layer Deposition: Nucleation and Growth of TiO2 on Planar Substrates and in Nanoporous Films. *J. Phys. Chem. C* **2011**, *115* (14), 6605–6610. https://doi.org/10.1021/jp111314b.

(26) Detavernier, C.; Dendooven, J.; Pulinthanathu Sree, S.; Ludwig, K. F.; Martens, J. A. Tailoring Nanoporous Materials by Atomic Layer Deposition. *Chemical Society Reviews*. The Royal Society of Chemistry October 17, 2011, pp 5242–5253. https://doi.org/10.1039/c1cs15091j.

(27) Kozen, A. C.; Pearse, A. J.; Lin, C. F.; Schroeder, M. A.; Noked, M.; Lee, S. B.; Rubloff, G. W. Atomic Layer Deposition and in Situ Characterization of Ultraclean Lithium Oxide and Lithium Hydroxide. *J. Phys. Chem. C* **2014**, *118* (48), 27749–27753. https://doi.org/10.1021/jp509298r.

(28) Labyedh, N.; Mattelaer, F.; Detavernier, C.; Vereecken, P. M. 3D LiMn2O4 Thin-Film Electrodes for High Rate All Solid-State Lithium and Li-Ion Microbatteries. *J. Mater. Chem. A* **2019**, *7* (32), 18996–19007. https://doi.org/10.1039/c9ta03703a.

(29) Maino, G.; Carleer, R.; Marchal, W.; Bonneux, G.; Hardy, A.; Van Bael, M. K. Remarkable Lowering in the Synthesis Temperature of LiMn2O4: Via Citrate Solution-Gel Synthesis Facilitated by Ethanol. *Dalt. Trans.* **2017**, *46* (43), 14934–14946. https://doi.org/10.1039/c7dt03100a.

(30) Lee, J. H.; Kim, J. M.; Kim, J. H.; Jang, Y. R.; Kim, J. A.; Yeon, S. H.; Lee, S. Y. Toward Ultrahigh-Capacity V2O5 Lithium-Ion Battery Cathodes via One-Pot Synthetic Route from Precursors to Electrode Sheets. *Adv. Mater. Interfaces* **2016**, *3* (14), 1–10. https://doi.org/10.1002/admi.201600173.
(31) Liu, J.; Zheng, Q.; Goodman, M. D.; Zhu, H.; Kim, J.; Krueger, N. A.; Ning, H.; Huang, X.; Liu, J.; Terrones, M.; et al. Graphene Sandwiched Mesostructured Li-Ion Battery Electrodes. *Adv. Mater.* **2016**, *28* (35), 7696–7702. https://doi.org/10.1002/adma.201600829.
(32) Wang, M.; Navrotsky, A. LiMO2 (M=Mn, Fe, and Co): Energetics, Polymorphism and Phase Transformation. *J. Solid State Chem.* **2005**, *178* (4), 1230–1240. https://doi.org/10.1016/j.jssc.2005.01.028.
(33) Cupid, D. M.; Reif, A.; Seifert, H. J. Enthalpy of Formation of Li1+xMn2-XO4 (0 < x < 0.1) Spinel Phases. *Thermochim. Acta* **2015**, *599*, 35–41. https://doi.org/10.1016/j.tca.2014.11.003.
(34) Knyazev, A. V; Mączka, M.; Smirnova, N. N.; Knyazeva, S. S.; Chernorukov, N. G.; Ptak, M.; Shushunov, A. N. Study of the Phase Transition and Thermodynamic Functions of LiMn2O4. *Thermochim. Acta* **2014**, *593*, 58–64. https://doi.org/http://dx.doi.org/10.1016/j.tca.2014.08.020.
(35) Cupid, D. M.; Li, D.; Gebert, C.; Reif, A.; Flandorfer, H.; Seifert, H. J. Enthalpy of Formation and Heat Capacity of Li2MnO3. *J. Ceram. Soc. Japan* **2016**, *124* (10), 1072–1082. https://doi.org/10.2109/jcersj2.16116.
(36) Du, T.; Xu, B.; Wu, M.; Liu, G.; Ouyang, C. Insight into the Vibrational and Thermodynamic Properties of Layered Lithium Transition-Metal Oxides LiMO2 (M = Co, Ni, Mn): A First-Principles Study. *J. Phys. Chem. C* **2016**, *120* (11), 5876–5882. https://doi.org/10.1021/acs.jpcc.5b11891.
(37) Yabuuchi, N.; Kim, Y.-T.; Li, H. H.; Shao-Horn, Y. Thermal Instability of Cycled LixNi0.5Mn0.5O2 Electrodes: An in Situ Synchrotron X-Ray Powder Diffraction Study. *Chem. Mater.* **2008**, *20*, 4936–4951.
(38) Kristin, P. Materials Data on LiMnO2 (SG:12) by Materials Project. 2014. https://doi.org/10.17188/1302955.
(39) Gotcu, P.; Seifert, H. J. Thermophysical Properties of LiCoO2-LiMn2O4 Blended Electrode Materials for Li-Ion Batteries. *Phys. Chem. Chem. Phys.* **2016**, *18* (15), 10550–10562. https://doi.org/10.1039/c6cp00887a.
(40) Liu, J.; Lin, X.; Zhang, H.; Shen, Z.; Lu, Q.; Niu, J.; Li, J.; Braun, P. V. A Bee Pupa-Infilled Honeycomb Structure-Inspired Li2MnSiO 4 Cathode for High Volumetric Energy Density Secondary Batteries. *Chem. Commun.* **2019**, *55* (25). https://doi.org/10.1039/c9cc00729f.
(41) Zhang, H.; Yu, X.; Braun, P. V. Three-Dimensional Bicontinuous Ultrafast-Charge and-Discharge Bulk Battery Electrodes. *Nat. Nanotechnol.* **2011**, *6* (5), 277–281. https://doi.org/10.1038/nnano.2011.38.
(42) Lou, F.; Zhou, H.; Huang, F.; Vullum-Bruer, F.; Tran, T. D.; Chen, D. Facile Synthesis of Manganese Oxide/Aligned Carbon Nanotubes over Aluminium Foil as 3D Binder Free Cathodes for Lithium Ion Batteries. *J. Mater. Chem. A* **2013**, *1* (11), 3757–3767. https://doi.org/10.1039/c3ta00793f.
(43) Shaijumon, M. M.; Perre, E.; Daffos, B.; Taberna, P.-L.; Tarascon, J.-M.; Simon, P. Nanoarchitectured 3D Cathodes for Li-Ion Microbatteries. *Adv. Mater.* **2010**, *22* (44), 4978–4981. https://doi.org/10.1002/adma.201001922.
(44) Self, E. C.; McRen, E. C.; Wycisk, R.; Pintauro, P. N. LiCoO2-Based Fiber Cathodes for Electrospun Full Cell Li-Ion Batteries. *Electrochim. Acta* **2016**, *214*, 139–146. https://doi.org/10.1016/j.electacta.2016.08.033.
(45) Zhang, H.; Ning, H.; Busbee, J.; Shen, Z.; Kiggins, C.; Hua, Y.; Eaves, J.; Davis, J.; Shi, T.; Shao, Y. T.; et al. Electroplating Lithium Transition Metal Oxides. *Sci. Adv.* **2017**, *3* (5), 1–9. https://doi.org/10.1126/sciadv.1602427.
(46) Zhou, H.; Li, Y.; Zhang, J.; Kang, W.; Yu, D. Y. W. Low-Temperature Direct Synthesis of Layered m-LiMnO 2 for Lithium-Ion Battery Applications. *J. Alloys Compd.* **2016**, *659*, 248–254. https://doi.org/10.1016/j.jallcom.2015.11.038.